# Spatially resolved analysis of $K\alpha$ x-ray emission from plasmas induced by a femtosecond weakly relativistic laser pulse at various polarizations

G. Cristoforetti,[1,*] M. P. Anania,[1,†] A. Ya. Faenov,[2] A. Giulietti,[1] D. Giulietti,[3,4] S. B. Hansen,[5] P. Koester,[1] L. Labate,[1,4] T. Levato,[1,‡] T. A. Pikuz,[2] and L. A. Gizzi[1,4]

[1]*Intense Laser Irradiation Laboratory (ILIL), INO-CNR, Via G. Moruzzi 1, 56124 Pisa, Italy*

[2]*Quantum Beams Science Directorate, Japan Atomic Energy Agency, Kizu, Kyoto 619-0215, Japan and High Temperatures of Russian Academy of Sciences, Izhorskaja Street 13/19, Moscow, Russia*

[3]*Department of Physics "E. Fermi," University of Pisa, Largo B. Pontecorvo 3, 56127 Pisa, Italy*

[4]*INFN, Pisa Section, Largo B. Pontecorvo 3, 56127 Pisa, Italy*

[5]*Sandia National Laboratories, Albuquerque, New Mexico 87123, USA*

(Received 23 July 2012; revised manuscript received 15 November 2012; published 13 February 2013)

Spatially resolved $K$-shell spectroscopy is used here to investigate the interaction of an ultrashort laser pulse ($\lambda = 800$ nm, $\tau = 40$ fs) with a Ti foil under intense irradiation ($I\lambda^2 = 2 \times 10^{18}$ W $\mu$m$^2$ cm$^{-2}$) and the following fast electron generation and transport into the target. The effect of laser pulse polarization ($p$, $s$, and circular) on the $K\alpha$ yield and line shape is probed. The radial structure of intensity and width of the lines, obtained by a discretized Abel deconvolution algorithm, suggests an annular distribution of both the hot electron propagation into the target and the target temperature. An accurate modeling of $K\alpha$ line shapes was performed, revealing temperature gradients, going from a few eV up to 15–20 eV, depending on the pulse polarization. Results are discussed in terms of mechanisms of hot electron generation and of their transport through the preplasma in front of the target.

DOI: 10.1103/PhysRevE.87.023103 PACS number(s): 52.50.Jm, 32.70.Jz, 52.38.Dx, 52.38.Ph

## I. INTRODUCTION

One of the most important effects produced by the interaction of an intense laser pulse with a solid target is certainly the generation of hot suprathermal electrons, with energies spanning from a few tens of keV up to several MeV. According to experimental findings, their average temperature $T_{\rm hot}$ scales as $(I\lambda^2)^{1/3}$ in the irradiance range $10^{17}$–$10^{19}$ W cm$^{-2}$ [1], with energy conversion efficiency and electron beam divergence strongly depending on the experimental conditions [2]. The mechanisms of laser energy absorption and of hot electron generation, occurring in the plasma at the target surface, are determined by the laser-plasma interaction regime, as shown in numerous works [1–4]. At irradiances larger than $\sim 10^{18}$ W cm$^{-2}$, which can be easily reached by chirped pulsed amplification (CPA) laser systems, the quivering velocity of the electrons in the oscillating electromagnetic (e.m.) wave field exceeds their thermal velocity, so that relativistic effects become dominant. The energetic hot electrons (extending up to a few tens of MeV) produced in this regime can penetrate the dense matter and effectively heat it; therefore, if adequately collimated, they could be utilized for a number of applications, among them the ignition of a precompressed thermonuclear fuel, according to the fast ignition scheme to inertial confinement fusion (ICF) [5]. In this scheme, a massive collimated beam of MeV electrons, produced by the interaction of a $\sim$10 ps laser pulse at $\sim 10^{20}$ W cm$^{-2}$ with the precompressed pellet, delivers its energy to the compressed core, causing its ignition. Other potential applications of energetic electron beams propagating into the solid matter are the investigation of properties of warm dense matter, i.e., the calculation of opacity, which has strong relevance in astrophysics [6], or the production of short bursts of $K$-shell x rays [7] or x-ray lasers [8].

All of the above applications require satisfactory control of the energy spectrum and of the collimation of the hot electrons, which needs an adequate understanding of the mechanisms of their generation and transport through the plasma and the solid. Despite the large number of theoretical and experimental works and progress in the understanding of the relevant physics, a clear and general accepted framework of knowledge is not yet available because of the large number of physical processes involved, often interplaying, and because of their dependence on a large amount of experimental parameters, among them the laser irradiance, the pulse polarization, and the scale length of the plasma.

The situation is particularly complicated at irradiances around the threshold at which relativistic effects on electron dynamics become significant. This occurs at values of the normalized momentum of quivering electrons $a_0 = eE/m\omega_0 c = 0.85(I_{18}\lambda^2)^{1/2}$ around 1, where laser intensity $I_{18}$ is expressed in units of $10^{18}$ W cm$^{-2}$ and $\lambda$ in units of microns. In this intermediate irradiance regime ($a_0 \approx 1$), relativistic mechanisms of hot electron generation such as $J \times B$ heating, betatron oscillation, and laser wakefield acceleration (LWFA) coexist with mechanisms which are dominant at lower irradiances, such as collisional, resonance, or Brunel absorption.

The competition between electron heating mechanisms at $a_0 \approx 1$ was clearly shown by Li *et al.* [9], who focused linearly polarized laser pulses onto an Al foil and identified resonance absorption and $J \times B$ heating as the leading processes. Li *et al.* measured a two-temperature hot electron distribution

*Corresponding author.

†Present address: LNF-INFN, Via E. Fermi 40, 00044 Frascati (Roma), Italy.

‡Also at Dipartimento di Ingegneria Industriale, Università di Roma "Tor Vergata," Italy and Fyzikln stav AV R v.v.i., Praha, Czech Republic.

 

at subrelativistic intensities ($a_0 < 1$), turning in a single temperature distribution, coinciding for $s$- and $p$-polarized beams, for relativistic ones ($a_0 > 1$). At the same time, they found a maximum of the emission cone angle ($\theta \approx 80^\circ$) of forward hot electrons at $a_0 = 1$, due to the concomitance of different heating mechanisms, with respect to that obtained at lower ($\theta \approx 60^\circ$) and higher ($\theta \approx 35^\circ$) laser irradiances. The concomitance of different mechanisms in case of $p$-polarized laser pulses was found also by Cho *et al.* [10] by utilizing an irradiance $I\lambda^2 = 2 \times 10^{19}\,\mathrm{W}\,\mu\mathrm{m}^2\,\mathrm{cm}^{-2}$ ($a_0 \approx 3$). They observed two distinct emission regions of coherent transition radiation (for details on CTR technique, see Refs. [11,12]) produced by hot electron beams on the rear of an Al foil. Despite the relativistic interaction regime, Cho *et al.* found that the production of hot electrons by resonance absorption still dominates over the $J \times B$ heating by one order of magnitude.

In the case of circularly polarized beams, the mechanisms of laser absorption in the range near $a_0 \approx 1$ are different and less known. Here, the generation of hot electrons by ponderomotive $J \times B$ heating is almost missing since the oscillating component of ponderomotive force is suppressed and the secular cycle-averaged component, i.e., the radiation pressure, is still small at such irradiance [13]. On the other hand, when the beam incidence is not normal, an oscillating electric field along the density gradient is present and can produce plasma waves and hot electrons. Other absorption mechanisms proposed for circularly polarized beams relate to the so-called inverse Faraday effect (IFE) in the underdense plasma. According to IFE, when a circularly polarized beam propagates into a plasma, electrons absorb angular momentum and gyrate in circular orbits, inducing an axial magnetic field along the laser propagation direction, whose intensity depends on plasma electron density, laser irradiance, and the plasma wavelength. According to Zeng *et al.* [14], when the cyclotron resonance condition is satisfied, a strong absorption of laser energy occurs and hot electrons are generated. Kustyukov *et al.* [15] suggest that laser energy and momentum can be resonantly absorbed by electrons executing betatron oscillations in the ion channel, which could result in both the generation of the axial magnetic field (IFE) and of hot electrons. While dedicated experiments have confirmed the generation of an axial magnetic field into the plasma [16,17], the conditions for which it develops and how it affects laser absorption are however still poorly explored and understood.

In this complex framework describing the laser-plasma interaction at $a_0 \approx 1$, the scenario is made far more complex by the eventual presence of a preplasma with a sufficient scale length, which can drive plasma instabilities, as stimulated Raman scattering, two-plasmon decay, or stochastic heating, affecting the generation of hot electrons, both via a direct acceleration in the underdense plasma regions [18–21], and via the considerable reduction of laser energy reaching the critical density surface.

Beyond the mechanisms of the laser-plasma interaction, which determine the electron spectrum, their angular distribution, and their conversion efficiency, an issue of primary importance to be explored is also their propagation through the plasma and the solid target [22]. The trajectories of the electrons are in fact not only determined by the collisions with background ions but are strongly affected by instabilities [23–26], self-induced electric and magnetic fields, both in the plasma [27,28] and into the target [29], and refluxing into the target [30,31], which determine the shape and the direction of the electron beam. Self-induced electric fields also affect the penetration depth of hot electrons into the target, since the limited conductivity of the solid, especially for insulators, determines the maximum balancing return current of cold electrons, and thus the maximum hot electron current which is able to propagate [32,33]. It is thus clear that the experimental investigation of laser-plasma interaction mechanisms cannot be separated from the study of the electron transport, since both the issues are closely related.

In previous works that focused on the investigation of electron transport into Ti foils, we investigated the role of longitudinal resistivity gradients via proton detection behind the target [34], and the role of directional bremsstrahlung from fast electrons via high-resolution x-ray imaging [35]. In the present paper, we investigate the effect of laser pulse polarization, both linear and circular, on the generation of hot electrons and on their transport into the target. To this aim, an ultrashort laser pulse was focused in a mildly relativistic regime ($a_0 \approx 1$) onto a Ti foil and the hot electrons were detected indirectly by using spatially resolved $K\alpha$ spectroscopy [36]. The $K\alpha$ lines are emitted by fluorescence cascade of bound electrons, which have been knocked out from the $K$ shell by a collision with a hot electron. The dependence of the cross section of x-ray fluorescence on the electron energy, however, makes this diagnostics particularly efficient for electrons of a few tens of keV energy [37,38] and sensitive to refluxing into the target [39]. A particularly attractive feature of the technique is the possibility of deriving information about target heating and density, which is made possible by an accurate modeling of the lines [40].

$K$-shell spectroscopy was used here in a focusing spectrograph with spatial resolution of one dimension (FSSR-1D) configuration, which provides a spectrally and 1D spatially resolved mapping of the electron beam, which is temporally integrated in a few ps, corresponding to the time of reequilibration of the atomic levels. A discretized Abel deconvolution algorithm was then used to derive the radial dependence of the $K\alpha$ spectra, which gives information about both the two-dimensional (2D) spatially resolved emissivity and width of the lines.

The observed dependence of intensity and width of the $K\alpha$ lines on pulse polarization was finally discussed in terms of hot electron generation mechanisms, while their spatial structure was explained by considering their propagation into the preplasma.

## II. EXPERIMENTAL SETUP

The experiment was carried out at ILIL Laboratory in Pisa by using a Ti:sapphire laser system, which delivers 800 nm, 40 fs laser pulses at a maximum energy of 100 mJ. The polarization of the beam was varied by means of half-wave and quarter-wave plates, located after the pulse compressor, which results also in a pulse stretching to a duration of 52 fs. The main pulse was preceded by a 3 ns pedestal due to amplified spontaneous emission (ASE) at a measured contrast ratio of $4 \times 10^{-8}$. The beam quality parameter $M^2$ is $\sim$2. The

laser pulse was focused on the target at an angle of incidence of 15°, to a spot of 10 $\mu$m full width at half maximum (FWHM), using an off-axis parabolic mirror (effective $f/5$ number). The target, consisting of a 12-$\mu$m-thick Ti foil with transverse dimensions of 5 cm × 5 cm, was mounted on a three-axis translational stage system and moved laterally by 2 mm at each laser shot. The accuracy of laser focusing, checked online during the experiment by means of a CCD, was of ∼10 $\mu$m, which is significantly lower than the Rayleigh range.

The irradiance on the target was of $I\lambda^2 \approx 2 \times 10^{18}$ W $\mu$m$^2$ cm$^{-2}$ ($a_0 \approx 1$). The experiment was performed in a vacuum chamber at a residual air pressure of $\sim 10^{-3}$ mbar.

A spherically bent quartz crystal ($2d_{2130} = 3.082$ Å, first diffraction order, $R = 150$ mm), looking at the rear side of the target (angle of sight ∼10° from the normal) and placed 260 mm from it, was used in a FSSR-1D configuration [41] to detect Ti $K\alpha$ line emission from the target. This setup allows the simultaneous spectral dispersion of x-ray lines along the horizontal direction ($x$ axis on the CCD) and spatial resolution along the sagittal plane ($y$ axis on the CCD). Moreover, since the x-ray CCD detector (Andor DX 434) is located on the Rowland circle (129.1 mm from the Bragg crystal), the spectral resolution is not limited by the dimensions of the source. The estimated resolving power of the spectrometer was $\lambda/\Delta\lambda \sim 7500$, and the spatial resolution of the images was approximately 50 $\mu$m.

## III. RESULTS

### A. Preplasma dimensions

The estimation of preplasma extent at the arrival time of the main peak is crucial both for assessing the laser absorption mechanisms as well as for describing the propagation of hot electrons before they enter the solid target. The marked variation of the $K\alpha$ line intensity with pulse polarization, showed in the following sections, implies that the preplasma profile at densities near a critical density $n_c$ is planar (1D), i.e., the scale length $L = n/(\partial n/\partial x)$ at $n_c$ cannot be larger than the spot size (∼10 $\mu$m). When 2D effects prevail, in fact, the preplasma shape tends to become spherical and the oscillating electric field of the e.m. wave becomes orthogonal to $\nabla n$ (approaching $s$ polarization) for any linear beam polarization. These circumstances would lead to little dependence on polarization, which is in contrast with our observations.

To support this conclusion, we performed a simulation of preplasma by using the 2D hydrodynamic code POLLUX, by considering a 3 ns FHWM Gaussian pedestal, Gaussian distributed along the focal spot (10 $\mu$m FWHM), at a maximum irradiance of $8 \times 10^{10}$ W cm$^{-2}$. The code was originally written by Pert [42] to model high-intensity laser irradiation ($I > 10^{10}$ W cm$^{-2}$) of solid targets. In these conditions, only a small fraction of the laser pulse interacts with the solid target surface, because of the rapid formation of a plasma slab in front of it, and plasma thermodynamics can be described by an ideal gas equation of state. Laser energy is prevailingly absorbed into the flowing outward plasma by inverse bremsstrahlung up to the critical density surface, which is justified by the low irradiance regime. The prevalence of collisional absorption implies also that preplasma dimensions are not affected by the polarization of the ASE prepulse.

The resulting preplasma electron density contour and profile along the longitudinal direction, at the time of arrival of the main pulse, are shown in Fig. 1. In accordance with previous considerations, the simulation shows evidence of a scale length value of 3–4 $\mu$m at the critical density. However, a large plasma region with densities $10^{17}$–$10^{18}$ cm$^{-3}$ extends for 100–150 $\mu$m in the radial direction and for 150–250 $\mu$m along the normal to the surface; the importance of such a low density plasma for the propagation of hot electrons will be discussed below.

### B. Polarization effects on the $K\alpha$ spatially integrated emission

$K\alpha$ spectra (∼4.5 keV) from Ti ion fluorescence were acquired for $s$, $p$, and intermediate linearly polarized laser pulses as well as for circularly polarized ones. In each case, several measurements, each one including 100 laser shots, were performed. As an example, the raw image obtained by averaging 100 $p$-polarized laser pulses is reported in Fig. 2(a), where the horizontal and the vertical axes provide spectral dispersion and 1D spatial resolution, respectively. The resulting spectra for $p$, $s$, and circular ($O$) polarization, obtained by averaging 100 individual shots and after background removal,

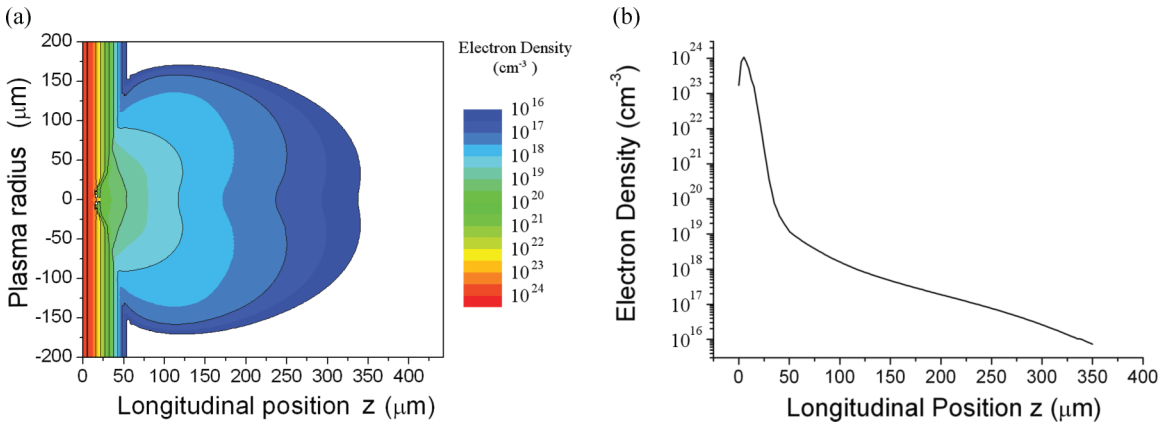


FIG. 1. (Color online) Preplasma density contour (a) and profile along the longitudinal direction at a plasma radius $r = 0$, at the time of arrival of the main pulse, obtained by the 2D hydrodynamic code POLLUX. In (a) the laser propagates along the $z$ direction from the right.

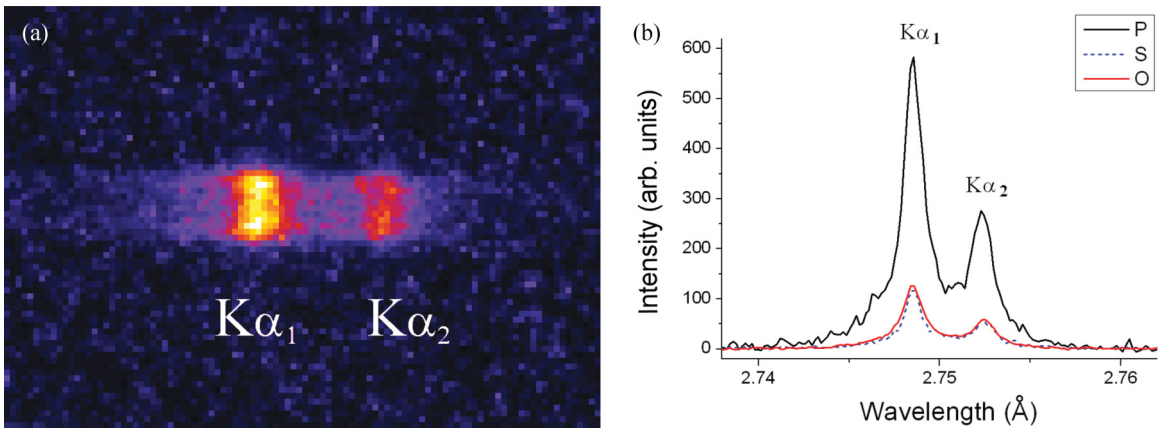


FIG. 2. (Color online) (a) $K\alpha$ raw image obtained by averaging 100 $p$-polarized laser pulses. The horizontal and vertical axes provide spectral dispersion and 1D spatial resolution, respectively. (b) $K\alpha$ spectra obtained by different laser pulse polarizations, and obtained by averaging 100 laser shots.

are reported in Fig. 2(b). In all the cases $K\alpha_1$ and $K\alpha_2$ lines are visible and well resolved. The ratio of $K\alpha_2$ to $K\alpha_1$ line intensity is in the range 0.47–0.50, which is in good agreement with the theoretical value of 0.5.

Both the intensity and the width of the lines show a marked dependence on the polarization of the laser pulse. In Fig. 3(a) the $K\alpha$ doublet intensity obtained with different polarizations, where the signal has been spatially and spectrally integrated, is reported. The largest intensity is obtained by using $p$-polarized pulses, with an evident decrease when $s$ polarization is approached. For $O$-polarized pulses, the signal is comparable to that obtained by $s$ pulses.

The width of the $K\alpha_1$ line in the different cases is reported in Fig. 3(b), obtained by fitting the $K\alpha$ doublet with two Lorentzian line shapes. Residue analysis of the line fitting shows a systematic inadequacy of a single Lorentzian profile to fit the bluetail of the $K\alpha_1$ line, because of a marked underestimation of the curve with respect to the experimental spectra. This result is due to the emergence of blueshifted satellites from ionized Ti [40] and will be discussed in the next section. Line fitting with a Lorentzian profile appears, however, sufficiently accurate to reproduce the peaks of the lines and to estimate their FWHM. The significant variation of linewidth shown in the figure denotes a different thermodynamic state of the source plasma, then following a different laser-plasma interaction. We observe that while in linear polarization the lines become narrower when $s$ polarization is approached, a circularly polarized beam produces $K\alpha$ linewidths comparable to those obtained by $p$ pulses.

### C. Spatial structure of $K\alpha$ emission

The data reported in Fig. 3 are spatially integrated and can provide only an estimation of the plasma temperature averaged in the emission region. A more detailed analysis of space-resolved spectra is then needed to extract information about the spatial variation of plasma temperature and the transport of fast electrons into the target.

The extent of the $K\alpha$ emission region can be obtained by measuring the FWHM of the emission along the $y$ axis of the CCD, i.e., in the sagittal plane of the spectrometer configuration. By fitting single shot spectra, we obtain a FWHM of $\sim$280 $\mu$m [relative standard deviation (RSD) of $\sim$10%], the same within the experimental uncertainty at a

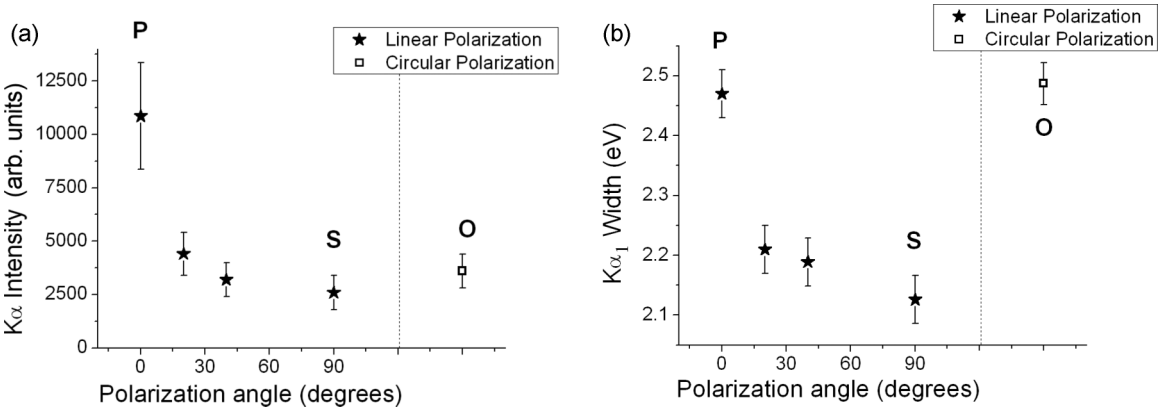


FIG. 3. Spectrally and spatially integrated intensity of (a) the $K\alpha$ doublet and (b) width of the $K\alpha_1$ line obtained with different laser pulse polarizations. The values are obtained by averaging three measurements of 100 shots, and the error bars represent the standard deviations obtained in different measurements.

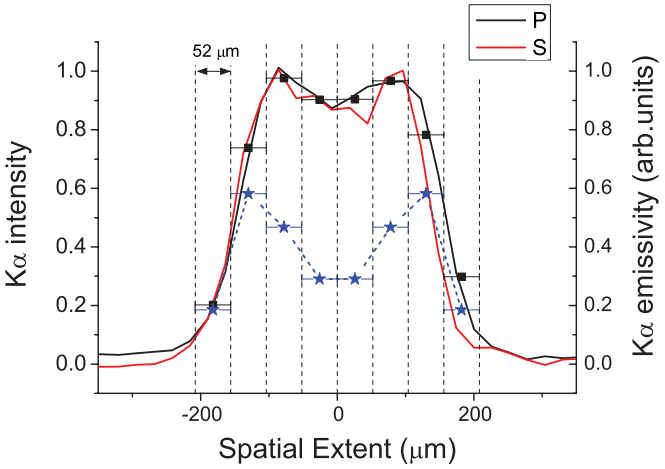


FIG. 4. (Color online) Spatial profile of $K\alpha$ doublet intensity, normalized at maximum intensity, obtained by averaging 100 laser shots for $p$ (black line) and $s$ (red/light gray line) polarizations. Black squares represent the discretized intensity values obtained by approximating the plasma as composed by four shells of thickness 52 $\mu$m, i.e., by performing a two-line binning. Blue stars represent the emissivity values (in a.u.) in different shells calculated by the deconvolution algorithm.

different pulse polarization. As shown in Fig. 4, the emission profile (spectrally integrated) along the $y$ axis exhibits a cylindrical symmetry and a dip in the center, where the signal is lower by ~10%–15% with respect to the maximum value of $K\alpha$ intensity, which is situated at a distance of ~90 $\pm$ 25 $\mu$m from it. The structure is present for all the polarizations used and confirmed in all the measurements series.

Detailed simulations performed with the x-ray tracing code ORTO, developed at ILIL Laboratory [43], accounting also for the crystal rocking curve, enabled us to exclude that the observed spatial profile was due to an experimental misalignment of the spectrometer.

The observed structure, although resolved in 1D along the vertical direction of the CCD ($y$ axis), is, however, still spatially integrated along its horizontal direction ($x$ axis, the spectral dispersive direction); thus, the spectra extracted at each $y$ position incorporate the contribution of radiation emitted at different $x$ positions (and radii) (see Fig. 5). Assuming a cylindrical symmetry of the emission, where the symmetry axis is perpendicular to the target surface ($z$ axis), a process of spectra deconvolution was performed, which finally provided the spectral emissivity, i.e., the number of photons per unit surface, in 2D as a function of the radius. As shown in literature [25], the cylindrical symmetry can be broken by

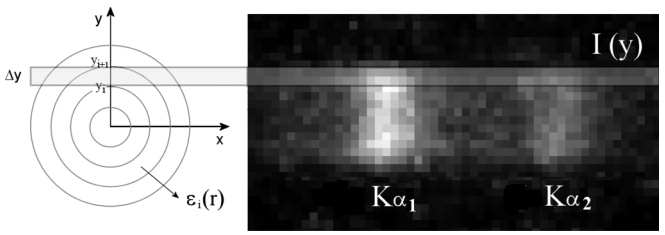


FIG. 5. Plasma "onion" model utilized for Abel deconvolution.

the filamentation of the beam, caused by plasma instabilities; however, such an effect should be here adequately overcome by averaging 100 CCD images. Given the lack of symmetry in the $z$ axis, it is not possible to spatially resolve the emission in 3D; however, since the depth of the target (12 $\mu$m) is much smaller than the $K\alpha$ emission diameter (~280 $\mu$m), and is smaller than the $K\alpha$ self-absorption distance, the plasma is considered here as a thin disk of a constant emissivity along $z$.

The algorithm utilized is a discrete version of the Abel inversion, similar to that used by Zastrau *et al.* [44] and described in detail in Refs. [45,46] (despite being used there for a different experimental configuration). In the algorithm a plasma slice (of depth $z$) is modeled as an "onion" structure (Fig. 5) composed of $n$ shells of constant thickness $\Delta r$ and characterized by a constant emissivity $\varepsilon_i(r)$. Clearly, the model approximates better the real plasma when $\Delta r$ is shorter than the scale length over which the parameters characterizing the plasma change significantly. The smallest thickness $\Delta r$ that can be used in the algorithm is the experimental spatial resolution $\Delta y$ of the apparatus. In our case, the spatial resolution is ~50 $\mu$m, so that we performed a vertical binning of the CCD image by averaging at least two lines (corresponding to ~52 $\mu$m) in each deconvolution process (see Fig. 5). After the binning, the spectra were averaged by pairs (the plasma was symmetrized) and slightly smoothed by a low-pass frequency filter to reduce the noise. Then, starting from the intensity (1D) at the border of the spot, which evidently includes only the contribution of the most external shell, the spectral emissivity (2D) of all the shells was calculated by considering the spectral intensity measured closer and closer to the center of the spot and subtracting the intensity derived from the external shells. During the deconvolution, the algorithm accounted for the geometrical fill factors of the shell portions along the horizontal line of integration.

In Fig. 4, the spectrally integrated emissivity values referring to $p$ polarization, obtained by approximating the plasma as composed of four plasma shells (where a vertical binning of 2 was used), are reported; by comparing the results with the intensity (1D) values at different vertical heights, which are spatially integrated along the $x$ axis, it is evident that the deconvoluted profile exhibits an even more enhanced dip in the center (signal reduction larger than 50%) and a slightly larger diameter of the maximum emission ring. A qualitatively similar spatial profile was also obtained in $s$ and $O$ polarization, showing no macroscopic changes.

The analysis of emissivity spectra also allowed the line shapes and widths at different plasma radii to be derived, which are important to infer the temperature distribution into the target. Here, however, the task was made more complicated by the noise present in the spectra, which is significantly amplified by the deconvolution algorithm. In order to reduce this drawback, a binning of three CCD lines was used, resulting in a plasma model of three shells of 78 $\mu$m thickness; an example of deconvoluted emissivity spectra with a binning of 3, obtained in $p$ polarization [for which the signal-to-noise (S/N) ratio is higher], is reported in Fig. 6(a). Despite the poor accuracy of the deconvoluted line profiles arising from the rough plasma approximation (here the shell thickness $\Delta r$ is larger than the length of intensity variation), and their

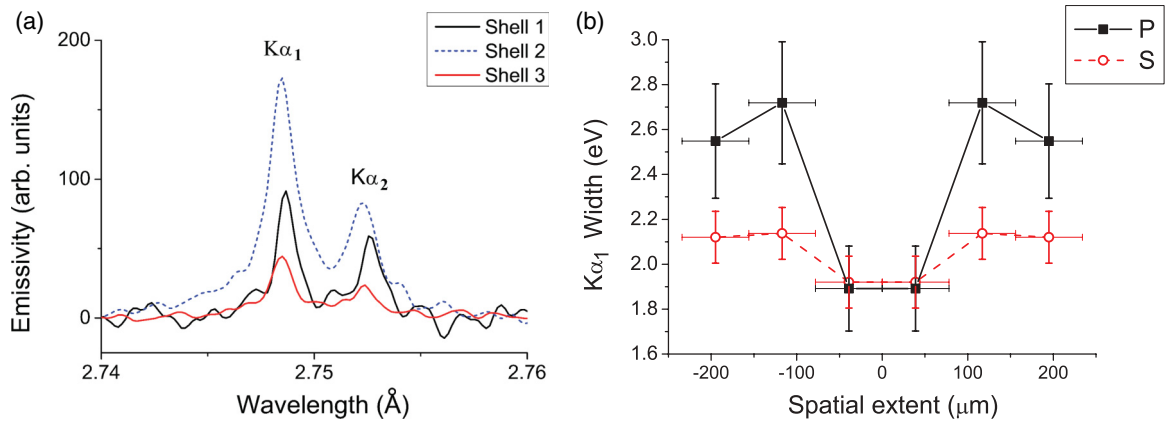


FIG. 6. (Color online) (a) Spectrum and (b) width of the $K\alpha_1$ line, obtained after a deconvolution by considering a three-shell plasma model.

unreliability for precise temperature evaluation, the emissivity spectra nevertheless can suggest trends of temperature and density values along the plasma radius. In this case, the width of the lines coming from the inner region, obtained by the deconvoluted spectra, was appreciably smaller than those coming from external shells [Fig. 6(b)]. Such a trend is visible in all the cases, but more evident in spectra obtained by $p$-polarized laser pulses where the S/N ratio is higher and the extent of variation of the width seems larger. This result would imply a lower bulk target temperature in the core of the $K\alpha$ emission region and a higher one in the ring of maximum emission. It is worth noting that the width of the Ti $K\alpha_1$ lines coming from the inner region (deconvoluted by the experimental broadening ~0.7 eV) is just a fraction of eV higher than the natural width of the line [47], suggesting that heating of the target in that region is small.

### D. Line modeling

An accurate modeling of $K\alpha$ line shapes was performed to extract information about the temperature and its distribution into the target. In order to reproduce the bluetail of the lines, described previously, it is necessary to calculate the detailed atomic structure and the charge state distribution of Ti ions. To this aim, we used the hybrid-structure collisional-radiative code SCRAM [48–50]. The modeled atomic structure includes states accessible by single-electron excitations from all shells of all ionization states up to a principal quantum number $n = 10$ and multiple-electron excitations from the valence and first inner shells up to $n = 6$. All of the standard processes of collisional excitation, ionization, radiative recombination, Auger and radiative decay, and the reverse rates are included, along with an ion sphere model of continuum lowering. A small fraction ($f < 1\%$) of suprathermal electrons was taken to exist in a hot Maxwellian distribution with $T_{\rm hot} \sim 10$ keV (there is little dependence on the exact temperature [51]); these electrons produce the $K$-shell holes that lead to $K\alpha$ emission. The collisional processes from bulk thermal electrons control the charge state distribution, thus providing a temperature diagnostic from the observed line structure [40]. The $K\alpha$ emission lines are broadened by thermal, natural, collisional, and approximate Stark [52] effects.

The $K$-shell emission due to the fluorescence cascade of electrons knocked out by the impact with hot electrons occurs within 10 ps, which can be estimated by the traveling time of fast electrons into the target and by the reequilibration time of levels by collisional-radiative models (1–10 ps) [53]. In this short time, the ions, moving on a hydrodynamic time scale, can be considered fixed, which justifies the solid state density utilized in the code.

The bulk-temperature dependence of the $K\alpha$ emission feature intensities and shapes from a solid-density Ti foil ($\rho_0 = 4.5$ g/cm$^3$) is shown in Fig. 7. As $T$ increases from <1 eV, thermal ionization of the valence electrons increases the average ion charge from its cold-metal $\langle Z \rangle \sim 3$ up to ~5 at 20 eV and ~10 at 100 eV. As the $3p$ electrons are ionized and multiply excited states are populated, the screening of the nucleus is reduced and $K\alpha$ emission lines shift to higher energies. The effect of increasing temperature initially manifests as a broadening of the $K\alpha$ feature, and for $T > 20$ eV, the broadened feature exhibits a global blueshift. No opacity effects were considered, as the optical depth of the $K\alpha$ line

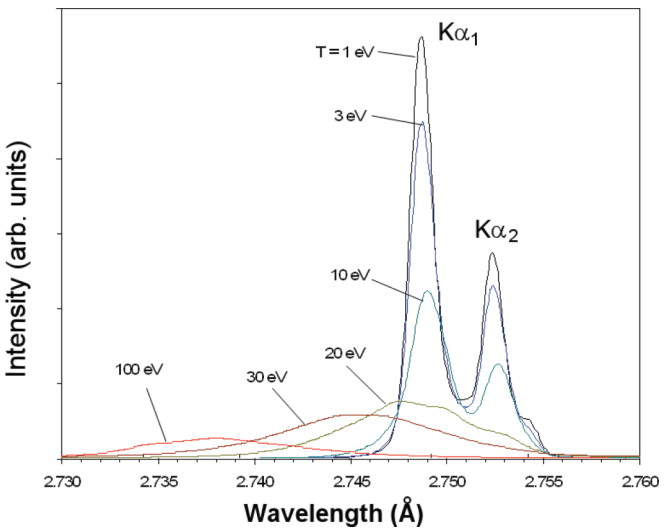


FIG. 7. (Color online) Dependence of solid-Ti $K\alpha$ emission on the bulk thermal plasma temperature $T$. The hot electron fraction is 0.1% and $T_{\rm hot} = 10$ keV.

along the instrumental line of sight is much less than unity, and time-dependent effects were not included due to the high electron density. It is not possible to achieve a satisfactory fitting of line profiles using the calculated emission profiles at a single temperature, because the narrow FWHM width of the lines (implying temperatures as low as 1–2 eV) is not compatible with the marked high-energy tail (which is due to blueshifted satellites of ionized Ti from hotter plasma regions, especially visible in the $K\alpha_1$ line).

The measured emission spectra thus imply spatial and possibly temporal temperature gradients in the emitting plasma. The relative contributions of temporal and spatial temperature variations are difficult to establish since it would require accurate particle-in-cell (PIC) simulations or dedicated experiments (e.g., able to decouple the two effects or focused to improve spatial resolution in Abel inversion). The spatially deconvoluted spectra described above establish the presence of radial gradients, suggesting a cold core surrounded by a hotter ring. Both the higher $K\alpha$ yield and larger linewidths in the outer ring suggest a larger density of hot electrons there; the derived emissivity profiles [Fig. 6(a)] suggest that the density of hot electrons in the outer ring is approximately two times higher than the hot electron density in the target center. Thus, we modeled the plasma assuming two plasma regions following the deconvolution presented in Fig. 4: a cold core of $\sim$100 $\mu$m radius with a bulk electron temperature $T \sim$ 1–3 eV and a hot electron fraction $f$ surrounded by an annulus with $\Delta r \sim 25$ $\mu$m, a higher $T \sim$ 15–20 eV, and a higher hot electron fraction $\sim 2f$ (the region around the ring is neglected because of its low emissivity). This two-region model results in a reasonably good fit of the time- and space-integrated experimental spectra, as shown in Fig. 8, and the spatially deconvolved emissivity profile given in Fig. 4. The $p$-polarized laser pulses are best fitted with higher temperatures and hot electron fractions than those obtained by $s$-polarized beams, which is in accordance with the intensity variations shown in Fig. 3. The hot electron fraction is not uniquely correlated with the derived temperature, suggesting there may be non-Joule heating mechanisms, temporal effects, or surface effects. Moreover, the dependence of efficiency of $K\alpha$ emission on the hot electron energy should also be considered for a more accurate determination of hot electron fractions at various polarizations. We note, too, that the given fits are not unique; other combinations of volumes, temperatures, and hot electron fractions could give similar results. However, the given parameters are a minimum set that can describe both the shapes and intensities of the emission features with reasonable confidence.

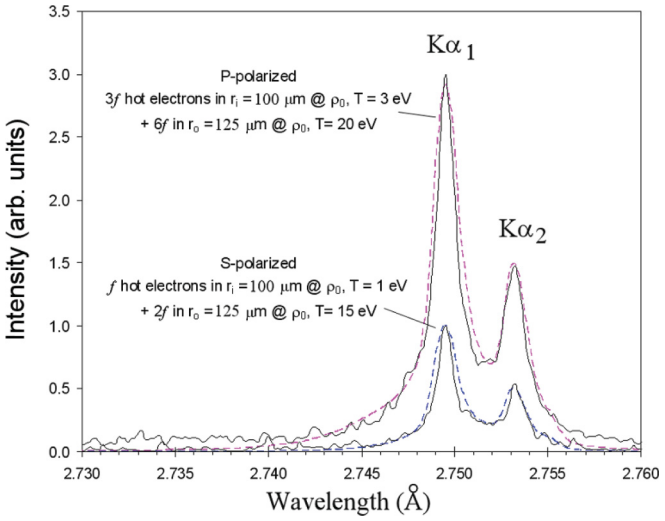


FIG. 8. (Color online) Space-resolved Ti $K\alpha$ emission from $s$- and $p$-polarized beam experiments (solid lines) modeled with a two-temperature plasma based on the intensity deconvolution given in Fig. 4 and the linewidth analysis given in Fig. 6: A cool, few-eV solid-density core with radius $\sim$100 $\mu$m is surrounded by a warm, solid-density annulus with thickness $\sim$25 $\mu$m, $T =$ 15–20 eV, and a higher hot electron fraction.

Finally, we remark on the possibility of a spatial temperature gradient along the longitudinal direction ($z$ axis), as it has been observed, e.g., in Ref. [40]. An axial gradient is due to the different stopping range of hot electrons of different energy, so that a large hot electron current (and then a large return current of background cold electrons) is present near the front surface, where all hot electrons contribute to it, and a minor one, only due to hotter electrons, propagates near the rear side (according to the electron stopping power, a 50 keV energy is needed to reach the rear of the target). Further measurements would have to be made to quantitatively assess the contribution of axial gradients to the overall signal.

In conclusion, the observed spectra are produced by a nonstationary and/or inhomogeneous temperature distribution inside the target. The fitting of the lines suggests the presence of regions of temperatures going from a few eV to 15–20 eV, depending on the laser pulse polarization. A modeling of two concentric regions can roughly reproduce the experimental spectra, although a more accurate description would account also for the longitudinal gradient and for the time dependence of temperature.

## IV. DISCUSSION

### A. Effect of laser pulse polarization on $K\alpha$ lines

The trends of $K\alpha$ line intensity and width shown in Figs. 3 and 8 are dictated by different mechanisms of hot electron generation at varying the laser pulse polarization. The multiplicity of mechanisms is driven by the irradiation regime ($a_0 \approx 1$), which lies in a region of transition between classical and relativistic electron dynamics during the laser-plasma interaction. For the interpretation of the results it is useful to bear in mind the values of the hot electron temperature (i.e., the slope temperature of the electron spectrum) predicted by Beg's scaling [1], experimentally derived by using $p$-polarized beams in a regime dominated by resonance absorption, and by the ponderomotive scaling, introduced by Wilks [3] for relativistic interaction, which does not depend on pulse polarization. Such values can be calculated by $T_{\rm hot}^{\rm Beg} = 0.215[I_{18}\lambda^2]^{1/3} \approx 233$ keV, and $T_{\rm hot}^{\rm pond} = m_e c^2[\sqrt{1+\frac{I_{18}\lambda^2}{2.8}} - 1] \approx 106$ keV, respectively, where laser intensity $I_{18}$ is expressed in units of $10^{18}$ W cm$^{-2}$ and $\lambda$ in units of microns. The lower value given by ponderomotive scaling is due to the still modest effectiveness of the $J \times B$ mechanism in the regime utilized.

The concomitance of different mechanisms is shown, in our case, by the different intensity of the $K\alpha$ lines measured for $s$- and $p$-polarized beams. In case of linear polarization, in fact, $J \times B$ heating does not depend on the direction of the $E$ field vector of the e.m. wave; so, when this mechanism becomes dominant (i.e., for $a_0 \gg 1$), the conversion efficiency and the spectrum of hot electrons generated by $s$ and $p$ beams tend to converge [54,55].

In $s$-polarized beams, $J \times B$ heating as well as plasma instabilities in the underdense plasma can generate hot electrons. The relevance of plasma instabilities is difficult to estimate, but can be significant, as suggested by the higher temperatures of hot electrons measured in the presence of a considerable preplasma [56] and obtained by PIC simulations [57,58]. Adam *et al.* [20] performed particle-in-cell simulations of laser pulse propagation ($I\lambda^2 = 2.6 \times 10^{18}$ W $\mu$m$^2$ cm$^{-2}$) in underdense and overdense plasma slabs of tens of microns, finding a strong pulse absorption (ranging from 50% to 90%), associated with plasma instabilities, resulting in electron energies up to tens of MeV.

When $p$-polarized beams are used, in addition to $J \times B$ heating and plasma instabilities, hot electrons are produced by resonance absorption or Brunel heating. Here, however, Brunel heating is not efficient because the preplasma scale length $L$ is larger than the laser wavelength $\lambda$. Therefore, we assume that the larger values of $K\alpha$ intensity and linewidth (Figs. 3 and 8) observed in $p$ polarization with respect to $s$ polarization is due to resonance absorption. Besides, it is possible that the generation of hot electrons by plasma instabilities may also be affected by pulse polarization, as shown, for example, for stochastic heating in Ref. [21], which could also contribute to the results obtained. In a previous work [59], where a Ti foil target was irradiated at $I\lambda^2 \approx 5 \times 10^{16}$ W $\mu$m$^2$ cm$^{-2}$, we observed a similar dependence of x-ray yield on pulse polarization; however, in that case, the rise of x-ray intensity from $s$ to $p$ polarization was larger than one order of magnitude, while it is only a factor 3–4 in the present work. The difference in the two experiments can be explained by the inefficiency of the $J \times B$ heating at $I\lambda^2 \approx 5 \times 10^{16}$ W $\mu$m$^2$ cm$^{-2}$, while the mechanism is expected to play a significant role in the present experiment, resulting in an increase of $K\alpha$ emission in the case of $s$ polarization.

$p$-polarized beams result also in a significantly larger width of the $K\alpha$ lines, which indicates a stronger heating of the target. A larger efficiency of laser energy conversion into hot electrons, due to the presence of resonance absorption, can explain this observation. Also the higher average electron energy for $p$-polarized beams, reported in numerous experiments [9,60] and PIC simulations [54], can lead to a higher target heating if electron refluxing plays a significant role.

$K\alpha$ spectra produced by $O$-polarized beam irradiation show a dual behavior, characterized by a low line intensity, comparable to $s$-polarized beams, but also by a linewidth comparable to $p$-polarized beam irradiation. In order to discuss this discrepancy, it is useful to review the processes affecting line intensity and linewidth. In case of sufficiently thick targets, the efficiency of $K\alpha$ emission versus the incidence electron energy does not trace the $K\alpha$ fluorescence cross section curve. In fact, the most energetic electrons downgrade their energy by collisions along their trajectories until they become low-energy electrons, so that ultimately they result in a number of $K\alpha$ photons proportional to their energy. At the opposite, in the case of a thin target (as the present), it was experimentally shown that the efficiency of $K\alpha$ emission is substantially given by the $K\alpha$ fluorescence cross section curve [61]. This is substantially justified by the outflow from the rear side of the foil [37] (where, however, a partial refluxing of the electrons can bring some change to this picture). This suggests that the electrons responsible for $K\alpha$ line emission are predominantly those in the low-energy side of the spectrum (in the range 10–50 keV), where the peak of the cross section is situated. Conversely, the width of the lines, depending on the charge state distribution of Ti ions, is related to the heating of the target, which is produced both by the collisions of hot electrons with the bound and free electrons into the solid as well as by the resistive Joule effect produced by the return currents of background electrons. In turn, to justify an efficient penetration of hot electrons into the solid, the return current $J_{\mathrm{ret}}$ should almost balance the direct hot electron current $J_{\mathrm{hot}}$, i.e., $J_{\mathrm{ret}} \approx J_{\mathrm{hot}}$ [22]. In the present experiment, considering the current density flowing into the target ($J_{\mathrm{hot}} \approx 2 \times 10^{10}$ A cm$^{-2}$, calculated according to the spatial distribution of $K\alpha$ emission; see below), the two contributions have a comparable weight. It is worth noting that, while the heating via direct hot electron collisions is more effectively produced by the less energetic electrons, similarly to the $K\alpha$ fluorescence emission, the heating rate by the resistive Joule effect does not depend directly on the electron spectrum but on the current density.

A different spatial propagation of the hot electrons induced by $s$- and $O$-polarized pulses could in principle explain the different linewidths observed, but this hypothesis conflicts with the measured $K\alpha$ spatial structure, which is similar in the two cases. It can be therefore hypothesized that the dual behavior of the intensity and width of the lines is produced by a different energy distribution of hot electrons obtained by $p$- and $O$-polarized beams, where in the latter case, a lower amount of electrons in the 10–50 keV range coexist with a large current density into the target, resulting in a significant heating.

The low efficiency of hot electron generation in the case of circularly polarized pulses predicted by PIC simulations [11,62], performed at an orthogonal beam incidence, and also some experimental results obtained at an oblique incidence [63], however, do not support the presence of a large current density. A different situation would occur if a resonant absorption of the e.m. wave in the longitudinal magnetic field produced by IFE [14,15] would play a significant role; such phenomena have been, however, poorly investigated until now and need experimental verification.

### B. $K\alpha$ emission spatial structure

The second issue that needs to be discussed is that which is relative to the $K\alpha$ emission spatial structure. The extent of $K\alpha$ fluorescence is much larger than the irradiated spot (by a factor of $\sim$28), which qualitatively agrees with other experiments showing considerable dimensions of the $K\alpha$ regions [64–67].

It is worth noting that an annular distribution of $K\alpha$ emission cannot be trivially produced by the Gaussian spatial profile of laser intensity. One, in fact, could assume that the

largest amount of low energetic electrons, which are more effective in driving $K\alpha$ line emission, was produced by the low-energy tail of the pulse spatial distribution. However, a rapid estimate of the amount and spectrum of electrons produced in each spatial position, by considering a constant efficiency conversion of 30–40% and a Maxwell distribution of electrons with the average temperature given by the Beg's law, shows that the amount of 10–50 keV electrons produced in the center of the focal spot is always greater than in its periphery. This rough estimation agrees with the results obtained by Kern *et al.* [64], focusing a 35 fs laser pulse at $I\lambda^2 \approx 2 \times 10^{19}$ W $\mu$m$^2$ cm$^{-2}$ onto a Ti foil, who measured the spatial distribution of the highest-energy electrons via CTR imaging and the bulk of hot electron population via spatially resolved $K\alpha$ spectroscopy. Their results show that the fastest electrons are distributed in a small central spot ($\sim$7 $\mu$m), but also the $K\alpha$ emission is peaked in the center despite extending into a much wider region ($\sim$50–100 $\mu$m). Also the hypothesis of an overionization of the central part of the spot would require multi-keV temperatures and must be discarded. It is thus evident that the annular distribution of $K\alpha$ emission needs a circular distribution of hot electrons, as confirmed by the higher temperatures found in the periphery of the spot.

Many papers report a measured annular distribution of electrons, in a wide range of experimental conditions, and suggest mechanisms for its formation, in some cases supported by theoretical modeling. A certain number of authors hypothesize mechanisms related to the transport of electrons into the target. Davies *et al.* [29] showed that for sufficiently large laser irradiances ($I\lambda^2 > 5 \times 10^{19}$ W $\mu$m$^2$ cm$^{-2}$) the toroidal magnetic fields generated into the target by the hot electron beam push the electrons toward the external higher resistivity regions, resulting in the hollowing of the beam. However, a large irradiance is required to generate a hot electron current density so large as to produce a low resistivity region in the central region. Koch *et al.* [53], using a 5 ps pulse at $I\lambda^2 = 3 \times 10^{19}$ W $\mu$m$^2$ cm$^{-2}$, observed annular x-ray images (of diameter 50–100 $\mu$m) from buried layers in CH targets and a columnar temperature distribution, with a larger heating at the edge of the column; following the 3D PIC-hybrid results of Taguchi *et al.* [24], they suggest that the annular pattern is related to a local growth of the Weibel instability. Storm *et al.* [25], focusing a 500 fs pulse at $I\lambda^2 \approx 10^{19}$ W $\mu$m$^2$ cm$^{-2}$ over metal targets, observed filamentlike structures distributed along an annular pattern (of diameter 5–35 $\mu$m, increasing with target thickness) from CTR imaging of the rear side emission. The authors suggest that the structure derives from a partial collimation of the initially divergent fast-electron beam produced by self-generated resistive magnetic fields; the hypothesis is supported by a 3D hybrid particle-in-cell simulation code [68].

All these mechanisms seem unfit to explain our results, because the penetration depth of low-energy electrons ($T_{\rm hot} <$ 100 keV) at a target temperature of 1–10 eV is much lower than the radius of the $K\alpha$ spot. The collisional stopping range of 50 and 100 keV electrons, calculated by means of the ESTAR program distributed by NIST, is in fact $\approx$15 and 45 $\mu$m, respectively. Moreover, if we hypothesize that hot electrons originate from a focal spot region of $\approx$10 $\mu$m diameter and then propagate into the target, we must account for the effects of the electric fields on the electron transport that in this case become dominant upon the collisional ones. According to Bell *et al.* [32] and considering the semiclassical term for the electrical conductivity (the Spitzer term is lower by a factor $10^3$ at $T = 1$ eV and by a factor 10 at $T = 10$ eV), the penetration depth of 100 keV energy electrons is $\approx$2 $\mu$m. Thus, in the case of electron transport into the target, such a wide region could be explained only by the propagation of MeV electrons, moving at large divergence or reaching the rear of the target and refluxing backward; in this case, however, most of the produced fast electrons, which have a lower energy, would stop at lower radii, which is not compatible with the ring structure observed. These considerations suggest that the measured dimensions and the annular distribution of $K\alpha$ emission are not explainable with mechanisms related to the electron transport into the target.

The transport of electrons inside the preplasma, where the Spitzer conductivity is larger than into the target, and the effect of self-generated electric and magnetic fields on electron trajectories, should then be considered.

Amiranoff *et al.* [65], using irradiances in the range $10^{15}$–$10^{16}$ W $\mu$m$^2$ cm$^{-2}$ over various planar targets, observed an annular $K\alpha$ emission region of diameter of the order of a millimeter, increasing with laser pulse duration. Results were explained by the presence of a toroidal magnetic field, surrounding the interaction region and produced by the usual $\nabla T \times \nabla n$ mechanism, which channels the fast electrons toward the edge of the plasma cloud. According to this interpretation, longer laser pulses result in larger plasmas and then in larger $K\alpha$ ring radii. Similar results have been obtained at higher irradiances ($I\lambda^2 \approx 10^{17}$–$10^{18}$ W $\mu$m$^2$ cm$^{-2}$) by Burgess *et al.* [27] and Paradkar *et al.* [69]. The thermoelectric toroidal magnetic field is expected to saturate at a few MG intensity, because of the advection term in the field generation equation [70], as verified by dedicated experiments [27,71,72]. The mechanism of hot electron transport toward the lateral plasma boundary was numerically modeled by Forslund *et al.* [73] and Fabro *et al.* [74]. More recently, in Ref. [69] a 3D-hybrid code was used to describe the trajectories of hot electrons in the presence of a preplasma, and the results were compared with experimental findings, performed at a laser irradiance $I\lambda^2 = 3 \times 10^{18}$ W $\mu$m$^2$ cm$^{-2}$). According to the simulation, a certain amount of hot electrons traveling through the electric sheath at the critical density surface is driven by the $E \times B$ drift along the radial direction, where the peak of the simulated azimuthal magnetic field is $\approx$0.21 MG. When electrons reach the lateral edge of the plasma, where both the magnetic field and plasma conductivity abruptly fall, they are pulled back toward the solid target by the thermoelectric magnetic fields and the self-generated electric fields. The sheath at the plasma edge is relevant when the density of traveling hot electrons becomes larger than the background density in the preplasma, so that the hot electron current cannot be neutralized anymore by the return currents of colder electrons; according to Ref. [69], this occurs in the $10^{17}$–$10^{18}$ cm$^{-3}$ electron density region, whose dimensions determine the radius of the electron ring. According to the simulation, the spectral distribution of electrons that reenter into the solid has a lower average temperature, since the hottest electrons are not affected by the electric sheath at the plasma boundary or are less deviated by the toroidal magnetic field.

Both dimensions and the spatial structure of $K\alpha$ emission obtained in the present work can be satisfactorily described by this model. In fact, according to our hydrodynamic simulation, the density contour at $10^{17}$–$10^{18}$ W cm$^{-2}$ has a radius of ∼100–150 $\mu$m [Fig. 1(a)], which agrees with the dimensions of the $K\alpha$ ring. Moreover, the dimensions of the $K\alpha$ annular structure do not depend on laser pulse polarization, which can be explained by the fact that the dimensions of the emission ring coincide with those of the preplasma, that, in turn, do not depend on laser beam polarization. Finally, in our results the ring is situated at the border of the emission spot, and the intensity steeply falls around it, which agrees with the inhibition of the motion of the less energetic electrons out of the plasma boundary. Also the low energy of electrons entering into the target (lower than ∼80 keV, according to Ref. [63]) agrees with the peak of cross section for Ti $K\alpha$ fluorescence at 10–50 keV.

## V. CONCLUSIONS

Spatially resolved $K\alpha$ spectroscopy was utilized to investigate the dependence of hot electron generation and transport on laser pulse polarization in the mildly relativistic ($a_0 \approx 1$) laser-plasma interaction regime.

While the polarization is found to affect significantly the amount and energetic spectrum of the hot electrons, as well as the resulting heating of the target, it seems not to influence their transport into the solid. The largest $K\alpha$ intensity measured in the case of $p$-polarized pulses suggests that resonance absorption is still dominant in this regime, even if the $K\alpha$ signal obtained for $s$ polarization shows that $J \times B$ heating and/or plasma instabilities are also present. The higher efficiency of hot electron generation in the case of $p$-polarized beams produces also a slightly higher temperature in the target compared to $s$-polarized beams, with maximum values of $T \sim 20$ eV versus $T \sim 15$ eV. Results obtained with circularly polarized pulses could be explained by a different energetic spectrum of hot electrons with respect to those produced by linearly polarized pulses. However, the identification of laser absorption mechanisms for $O$-polarized pulses is not a trivial task, because of the still limited knowledge in the field; further investigations are needed to study the generation of hot electrons by mechanisms related to the inverse Faraday effect. Generation mechanisms related to plasma instabilities in the underdense plasma region are possible in all the cases and could result in a large absorption of pulse energy, according to the literature; however, they are difficult to quantify here.

The 2D spatial structure of $K\alpha$ emissivity, calculated by a discretized Abel deconvolution algorithm, gives evidence of an annular region of ∼200 $\mu$m diameter (∼20 times larger than the focusing laser dimensions), where both the intensity and the width of the $K\alpha$ emission lines are larger. The ring structure found for the $K\alpha$ linewidth is a strong indication of the spatial distribution of the plasma temperature and suggests that hot electrons propagate into the target mainly along the ringlike structure. Accurate modeling of measured $K\alpha$ line shapes can satisfactorily reproduce the observed spectra, by supposing a hot ring of ∼200 $\mu$m diameter and 25 $\mu$m thickness with $T \sim$ 15–20 eV, surrounding an inner colder region with $T \sim$ 1–3 eV. A gradient of temperature along the target depth could also be present, due to the different penetration depths of hot electrons of different energies. The annular structure of $K\alpha$ emission is compatible with a model of electron transport into the preplasma which accounts for the self-generated electric and magnetic fields. According to the model, the electrons are drifted laterally by the $E \times B$ force, and then pulled back toward the target at the lateral borders of the plasma, where the plasma conductivity significantly drops. Finally we want to remark that the present qualitative interpretation of the phenomena observed, which seems able to explain the experimental results, should be corroborated by a self-consistent simulation, including laser-plasma interaction modeling, hot electron generation, and propagation into the preplasma and into the target. This work is, however, outside the scope of this paper.

## ACKNOWLEDGMENTS

This work was partially funded by the HiPER programme and by the MIUR-PRIN 2009 "Fusione a confinamento inerziale via laser [...]." A.Y.F. and T.A.P. were funded by INFN FAI funds for participation in the experimental campaign at ILIL laboratory.

[1] F. N. Beg, A. R. Bell, A. E. Dangor, C. N. Danson, A. P. Fews, M. E. Glinsky, B. A. Hammel, P. Lee, P. A. Norreys, and M. Tatarakis, Phys. Plasmas **4**, 447 (1997).

[2] J. S. Green, V. M. Ovchinnikov, R. G. Evans, K. U. Akli, H. Azechi, F. N. Beg, C. Bellei, R. R. Freeman, H. Habara, R. Heathcote, M. H. Key, J. A. King, K. L. Lancaster, N. C. Lopes, T. Ma, A. J. MacKinnon, K. Markey, A. McPhee, Z. Najmudin, P. Nilson, R. Onofrei, R. Stephens, K. Takeda, K. A. Tanaka, W. Theobald, T. Tanimoto, J. Waugh, L. Van Woerkom, N. C. Woolsey, M. Zepf, J. R. Davies, and P. A. Norreys, Phys. Rev. Lett. **100**, 015003 (2008).

[3] S. C. Wilks and W. L. Kruer, IEEE J. Quantum Electron. **33**, 1954 (1997).

[4] P. Gibbon and E. Forster, Plasma Phys. Controlled Fusion **38**, 769 (1996).

[5] M. Tabak, J. Hammer, M. E. Glinsky, W. L. Kruer, S. C. Wilks, J. Woodworth, E. M. Campbell, M. D. Perry, and R. J. Mason, Phys. Plasmas **1**, 1626 (1994).

[6] H. Takabe, Prog. Theor. Phys. Suppl. **143**, 202 (2001).

[7] W. Lu, M. Nicoul, U. Shymanovich, A. Tarasevitch, P. Zhou, K. Sokolowski-Tinten, D. von der Linde, M. Mašek, P. Gibbon, and U. Teubner, Phys. Rev. E **80**, 026404 (2009).

[8] F. Gervais, P. Hennequin, A. Quemeneur, A. Truc, A. L. Pecquet, C. Laviron, and P. Devynck, Plasma Phys. Controlled Fusion **39**, 43 (1997).

[9] Y. T. Li, J. Zhang, Z. M. Sheng, J. Zheng, Z. L. Chen, R. Kodama, T. Matsuoka, M. Tampo, K. A. Tanaka, T. Tsutsumi, and T. Yabuuchi, Phys. Rev. E **69**, 036405 (2004).

[10] B. I. Cho, J. Osterholz, A. C. Bernstein, G. M. Dyer, A. Karmakar, A. Pukhov, and T. Ditmire, Phys. Rev. E **80**, 055402 (2009).

[11] S. D. Baton, J. J. Santos, F. Amiranoff, H. Popescu, L. Gremillet, M. Koenig, E. Martinolli, O. Guilbaud, C. Rousseaux, M. R. Le Gloahec, T. Hall, D. Batani, E. Perelli, F. Scianitti, and T. E. Cowan, Phys. Rev. Lett. **91**, 105001 (2003).

[12] H. Popescu, S. D. Baton, F. Amiranoff, C. Rousseaux, M. Rabec Le Gloahec, J. J. Santos, L. Gremillet, M. Koenig, E. Martinolli, T. Hall, J. C. Adam, A. Heron, and D. Batani, Phys. Plasmas **12**, 063106 (2005).

[13] T. V. Liseikina, D. Prellino, F. Cornolti, and A. Macchi, IEEE Trans. Plasma Sci. **36**, 1866 (2008).

[14] G. Zeng, Phys. Plasmas **7**, 1539 (2000).

[15] I. Yu. Kostyukov, G. Shvets, N. J. Fisch, and J. M. Rax, Phys. Plasmas **9**, 636 (2002).

[16] Y. Horovitz, S. Eliezer, A. Ludmirsky, Z. Henis, E. Moshe, R. Shpitalnik, and B. Arad, Phys. Rev. Lett. **78**, 1707 (1997).

[17] Z. Najmudin, M. Tatarakis, A. Pukhov, E. L. Clark, R. J. Clarke, A. E. Dangor, J. Faure, V. Malka, D. Neely, M. I. K. Santala, and K. Krushelnick, Phys. Rev. Lett. **87**, 215004 (2001).

[18] A. Modena, Z. Najmudin, A. E. Dangor, C. E. Clayton, K. A. Marsh, C. Joshi, V. Malka, C. B. Darrow, C. Danson, D. Neely, and F. N. Walsh, Nature (London) **377**, 606 (1995).

[19] H. Figueroa, C. Joshi, H. Azechi, N. A. Ebrahim, and K. Estabrook, Phys. Fluids **27**, 1887 (1984).

[20] J. C. Adam, A. Héron, S. Guérin, G. Laval, P. Mora, and B. Quesnel, Phys. Rev. Lett. **78**, 4765 (1997).

[21] Z-M Sheng, K. Mima, J. Zhang, and J. Meyer-ter-Vehn, Phys. Rev. E **69**, 016407 (2004).

[22] D. Batani, Laser Part. Beams **20**, 321 (2002).

[23] E. W. Weibel, Phys. Rev. Lett. **2**, 83 (1959).

[24] T. Taguchi, T. M. Antonsen, Jr., C. S. Liu, and K. Mima, Phys. Rev. Lett. **86**, 5055 (2001).

[25] M. Storm, A. A. Solodov, J. F. Myatt, D. D. Meyerhofer, C. Stoeckl, C. Mileham, R. Betti, P. M. Nilson, T. C. Sangster, W. Theobald, and C. Guo, Phys. Rev. Lett. **102**, 235004 (2009).

[26] M. Manclossi, J. J. Santos, D. Batani, J. Faure, A. Debayle, V. T. Tikhonchuk and V. Malka, Phys. Rev. Lett. **96**, 125002 (2006).

[27] M. D. J. Burgess, B. Luther-Davies, and K. A. Nugent, Phys. Fluids **28**, 2286 (1985).

[28] L. A. Gizzi, A. J. Mackinnon, D. Riley, S. M. Viana, and O. Willi, Laser Part. Beams **13**, 511 (1995).

[29] J. R. Davies, J. S. Green, and P. A. Norreys, Plasma Phys. Controlled Fusion **48**, 1181 (2006).

[30] G. Nersisyan, M. Makita, K. McKeever, T. Dzelzainis, S. White, E. Nedanovska, B. Kettle, R. Nicholl, G. Williams, D. Riley, and C. L. S. Lewis, Phys. Rev. E **85**, 056415 (2012).

[31] E. Martinolli, M. Koenig, S. D. Baton, J. J. Santos, F. Amiranoff, D. Batani, E. Perelli-Cippo, F. Scianitti, L. Gremillet, R. Mélizzi, A. Decoster, C. Rousseaux, T. A. Hall, M. H. Key, R. Snavely, A. MacKinnon, R. R. Freeman, J. A. King, R. Stephens, D. Neely, and R. J. Clarke, Phys. Rev. E **73**, 046402 (2006).

[32] A. R. Bell, J. R. Davies, S. Guerin, and H. Ruhl, Plasma Phys. Controlled Fusion **39**, 653 (1997).

[33] F. Pisani, A. Bernardinello, D. Batani, A. Antonicci, E. Martinolli, M. Koenig, L. Gremillet, F. Amiranoff, S. Baton, J. Davies, T. A. Hall, D. Scott, P. Norreys, A. Djaoui, C. Rousseaux, P. Fews, H. Bandulet, and H. Pepin, Phys. Rev. E **62**, R5927 (2000).

[34] L. A. Gizzi, S. Betti, E. Forster, D. Giulietti, S. Hofer, P. Koster, L. Labate, R. Lotzsch, A. P. L. Robinson, and I. Uschmann, Phys. Rev. ST Accel. Beams **14**, 011301 (2011).

[35] F. Zamponi, A. Lubcke, T. Kampfer, I. Uschmann, E. Forster, A. P. L. Robinson, A. Giulietti, P. Koster, L. Labate, T. Levato, and L. A. Gizzi, Phys. Rev. Lett. **105**, 085001 (2010).

[36] R. B. Stephens, R. A. Snavely, Y. Aglitskiy, F. Amiranoff, C. Andersen, D. Batani, S. D. Baton, T. Cowan, R. R. Freeman, T. Hall, S. P. Hatchett, J. M. Hill, M. H. Key, J. A. King, J. A. Koch, M. Koenig, A. J. MacKinnon, K. L. Lancaster, E. Martinolli, P. Norreys, E. Perelli-Cippo, M. Rabec Le Gloahec, C. Rousseaux, J. J. Santos, and F. Scianitti, Phys. Rev. E **69**, 066414 (2004).

[37] F. Ewald, H. Schwoerer, and R. Sauerbrey, Europhys. Lett. **60**, 710 (2002).

[38] A. G. Zhidkov, A. Sasaki, I. Fukumoto, T. Tajima, T. Auguste, P. D. Oliveira, S. Hulin, P. Monot, A. Ya. Faenov, T. A. Pikuz, and I. Yu. Skobelev, Phys. Plasmas **8**, 3718 (2001).

[39] V. M. Ovchinnikov, G. E. Kemp, D. W. Schumacher, R. R. Freeman, and L. D. Van Woerkom, Phys. Plasmas **18**, 072704 (2011).

[40] S. B. Hansen, A. Ya. Faenov, T. A. Pikuz, K. B. Fournier, R. Shepherd, H. Chen, K. Widmann, S. C. Wilks, Y. Ping, H. K. Chung, A. Niles, J. R. Hunter, G. Dyer, and T. Ditmire, Phys. Rev. E **72**, 036408 (2005).

[41] F. Blasco, C. Stenz, F. Salin, A. Ya. Faenov, A. I. Magunov, T. A. Pikuz, and I. Yu. Skobelev, Rev. Sci. Instrum. **72**, 1956 (2001).

[42] G. J. Pert, J. Plasma Physics **41**, 263 (1989).

[43] L. Labate, M. Galimberti, A. Giulietti, D. Giulietti, L. A. Gizzi, P. Koster, S. Laville, and P. Tomassini, Laser Part. Beams **22**, 253 (2004).

[44] U. Zastrau, A. Sengebusch, P. Audebert, E. Brambrink, R. R. Fäustlin, T. Kämpfer, E. Kroupp, R. Loetzsch, Y. Maron, H. Reinholz, G. Röpke, E. Stambulchik, I. Uschmann, and E. Förster, High Energy Density Phys. **7**, 47 (2011).

[45] M. Corsi, G. Cristoforetti, M. Giuffrida, M. Hidalgo, S. Legnaioli, V. Palleschi, A. Salvetti, E. Tognoni, and C. Vallebona, Spectrochim. Acta, Part B **59**, 723 (2004).

[46] G. Cristoforetti, S. Legnaioli, V. Palleschi, A. Salvetti, E. Tognoni, and P. Tomassini, Spectrochim. Acta, Part B **60**, 888 (2005).

[47] D. F. Anagnostopoulos, D. Gotta, P. Indelicato, and L. M. Simons, Phys. Rev. Lett. **91**, 240801 (2003).

[48] S. B. Hansen, J. Bauche, C. Bauche-Arnoult, and M. F. Gu, High Energy Density Phys. **3**, 109 (2007).

[49] S. B. Hansen, J. Bauche, and C. Bauche-Arnoult, High Energy Density Phys. **7**, 27 (2011).

[50] S. B. Hansen, Can. J. Phys. **89**, 633 (2011).

[51] S. B. Hansen and A. S. Shlyaptseva, Phys. Rev. E **70**, 036402 (2004).

[52] E. Stambulchik and Y. Maron, J. Phys. B **41**, 095703 (2008).

[53] J. A. Koch, M. H. Key, R. R. Freeman, S. P. Hatchett, R. W. Lee, D. Pennington, R. B. Stephens, and M. Tabak, Phys. Rev. E **65**, 016410 (2001).

[54] S. C. Wilks, W. L. Kruer, M. Tabak, and A. B. Langdon, Phys. Rev. Lett. **69**, 1383 (1992).

[55] V. V. Bol'shakov, A. A. Vorob'ev, D. S. Uryupina, K. A. Ivanov, N. Morshedian, R. V. Volkov, and A. B. Savel'ev, Quantum Electron. **39**, 669 (2009).
[56] G. Malka, M. M. Aleonard, J. F. Chemin, G. Claverie, M. R. Harston, J. N. Scheurer, V. Tikhonchuk, S. Fritzler, V. Malka, P. Balcou, G. Grillon, S. Moustaizis, L. Notebaert, E. Lefebvre, and N. Cochet, Phys. Rev. E **66**, 066402 (2002).
[57] H.-b. Cai, K. Mima, A. Sunahara, T. Johzaki, H. Nagatomo, S.-p. Zhu, and X. T. He, Phys. Plasmas **17**, 023106 (2010).
[58] B. S. Paradkar, M. S. Wei, T. Yabuuchi, R. B. Stephens, M. G. Haines, S. I. Krasheninnikov, and F. N. Beg, Phys. Rev. E **83**, 046401 (2011).
[59] L. Labate, M. Galimberti, A. Giulietti, D. Giulietti, P. Koster, P. Tomassini, and L. A. Gizzi, Appl. Phys. B **86**, 229 (2007).
[60] A. Fukumi, M. Nishiuchi, H. Daido, Z. Li, A. Sagisaka, K. Ogura, S. Orimo, M. Kado, Y. Hayashi, M. Mori, S. V. Bulanov, T. Esirkepov, K. Nemoto, Y. Oishi, T. Nayuki, T. Fujii, A. Noda, and S. Nakamura, Phys. Plasmas **12**, 100701 (2005).
[61] C. E. Dick, A. C. Lucas, J. M. Motz, R. C. Placious, and J. H. Sparrow, J. Appl. Phys. **44**, 815 (1973).
[62] A. Henig, S. Steinke, M. Schnurer, T. Sokollik, R. Horlein, D. Kiefer, D. Jung, J. Schreiber, B. M. Hegelich, X. Q. Yan, J. Meyer-ter-Vehn, T. Tajima, P. V. Nickles, W. Sandner, and D. Habs, Phys. Rev. Lett. **103**, 245003 (2009).
[63] Z. Li, H. Daido, A. Fukumi, S. V. Bulanov, A. Sagisaka, K. Ogura, A. Yogo, M. Nishiuchi, S. Orimo, M. Mori, Y. Oishi, T. Nayuki, T. Fujii, K. Nemoto, S. Nakamura, A. Noda, I. W. Choi, J. H. Sung, D.-K. Ko, and J. Lee, Phys. Lett. A **369**, 483 (2007).
[64] J. Kern, S. Feldman, I. Kim, G. Dyer, B. I. Cho, A. C. Bernstein, and T. Ditmire, High Energy Density Phys. **8**, 60 (2012).
[65] F. Amiranoff, K. Eidmann, R. Sigel, R. Fedosejevs, A. Maaswinkel, Y.-l. Teng, J. D. Kilkenny, J. D. Hares, D. K. Bradley, B. J. MacGowan, and T. J. Goldsack, J. Phys. D: Appl. Phys. **15**, 2463 (1982).
[66] D. C. Eder, G. Pretzler, E. Fill, K. Eidmann, and A. Saemann, Appl. Phys. B **70**, 211 (2000).
[67] Ch. Reich, I. Uschmann, F. Ewald, S. Dusterer, A. Lubcke, H. Schwoerer, R. Sauerbrey, E. Forster, and P. Gibbon, Phys. Rev. E **68**, 056408 (2003).
[68] A. A. Solodov, M. Storm, J. F. Myatt, R. Betti, D. D. Meyerhofer, P. M. Nilson, W. Theobald, and C. Stoeckl, J. Phys.: Conf. Ser. **244**, 022063 (2010).
[69] B. S. Paradkar, M. S. Wei1, T. Yabuuchi, R. B. Stephens, J. T. Larsen, and F. N. Beg, Plasma Phys. Controlled Fusion **52**, 125003 (2010).
[70] C. E. Max, W. M. Manheimer, and J. J. Thomson, Phys. Fluids **21**, 128 (1978).
[71] J. A. Stamper, E. A. McLean and B. H. Ripin, Phys. Rev. Lett. **40**, 1177 (1978).
[72] A. Raven, O. Willi, and P. T. Rumsby, Phys. Rev. Lett. **41**, 554 (1978).
[73] D. W. Forslund and J. U. Brackbill, Phys. Rev. Lett. **48**, 1614 (1982).
[74] R. Fabbro and P. Mora, Phys. Lett. A **90**, 48 (1982).